Journal of Materials Chemistry C

Band Gap and Electronic Structure of Defects in the Ternary Nitride BP_3N_6: Experiment and Theory

Journal:	*Journal of Materials Chemistry C*
Manuscript ID	TC-ART-12-2021-006009.R1
Article Type:	Paper
Date Submitted by the Author:	19-Mar-2022
Complete List of Authors:	de Boer, Tristan; University of Saskatchewan, Physics and Engineering Physics Al Fattah, Md Fahim; University of Saskatchewan, Physics and Engineering Physics Amin, M. Ruhul; University of Saskatchewan, Physics and Engineering Physics Ambach, Sebastian; University of Munich, Department of Chemistry Vogel, Sebastian; University of Munich, Department of Chemistry Schnick, Wolfgang; University of Munich, Department of Chemistry Moewes, Alexander; University of Saskatchewan, Physics and Engineering Physics

ARTICLE

Band Gap and Electronic Structure of Defects in the Ternary Nitride BP_3N_6: Experiment and Theory

Received 00th January 20xx,
Accepted 00th January 20xx

DOI: 10.1039/x0xx00000x

Tristan de Boer,*[a] Md. Fahim Al Fattah,[a] Muhammad Ruhul Amin,[a] Sebastian J. Ambach,[b] Sebastian Vogel,[b] Wolfgang Schnick,[b] and Alexander Moewes[a]

Recent advances in methods to access nitride systems by a high-pressure high-temperature approach have made possible the one-step synthesis of mixed ternary non-metal nitrides. As a prerequisite to use in a practical device, it is important to understand important bulk electronic properties, such as the band gap, as well as characterizing the presence and effect of defects that are present. In this work, the novel ternary nitride BP_3N_6 is studied using techniques sensitive to the partial electronic density of states, specifically X-ray absorption spectroscopy and X-ray emission spectroscopy. Complementary full-potential all-electron density functional theory (DFT) calculations allow important bulk electronic parameters, such as the band gap, to be elucidated. The band gap of BP_3N_6 has been determined to be 3.9 ± 0.2 eV and 4.1 ± 0.4 eV at the B K- and N K-edges, respectively. This is close to a theoretical value of 4.3 eV predicted by the PBEsol exchange-correlation functional and considerably less than a value of 5.8 eV predicted by the modified Becke-Johnson exchange-correlation functional. X-ray excited optical luminescence (XEOL) measurements are performed to interrogate the presence of point defects in this system. Together with DFT calculations, these measurements reveal the presence of nitrogen vacancies which lead to multiple mid-gap trap states.

1 Introduction

Non-metal nitrides, such as Si_3N_4, BN and P_3N_5, have a wide range of applications in today's industry, originating from their versatile and intriguing materials properties.[1-6] For example, phosphorus(V) nitride P_3N_5 serves as gate insulator material in MISFETs and has been discussed regarding its use as flame retardant and in pyrotechnics.[3-6] While binary nitrides are omnipresent, there are no industrial applications of ternary or higher compounds of this class, although they may even surpass the versatility of the binary compounds. The absence of ternary non-metal nitrides may be explained with their limited number of known compounds, however, probably much more important, with their elaborate multi-step synthesis. $SiPN_3$, for example, has been prepared in five synthetic steps starting from hexamethyldisilazane.[7] The rarity and complexity of synthesizing these makes characterizing new members of this class a topic of both fundamental and industrial interest. As a recent advance, Vogel *et al.* demonstrated in the prototype compound BP_3N_6 that a new high-pressure high-temperature one-step synthetic method, utilizing *in situ* generated HCl, opens easy access to new mixed ternary non-metal nitrides.[8]

To identify potential applications of novel ternary nitrides, their electronic properties must be well understood. This includes bulk properties, such as the band gap, and particularly dilute electronic properties, such as the presence and effect of intentional and unintentional defects as these can greatly affect the overall material performance in a device. In this work, we study the novel mixed ternary nitride BP_3N_6 that has been synthesized in a one-step high-pressure high-temperature approach. Both the bulk electronic properties and the presence of defects are probed using synchrotron radiation.

To address the bulk electronic properties, the unoccupied and occupied partial density of states (PDOS) of BP_3N_6 were characterized using X-ray absorption spectroscopy (XAS) and X-ray emission spectroscopy (XES), respectively.[9-10] Both of these techniques rely on utilizing a bright, tunable X-ray source to excite core electrons to the conduction band and monitoring their subsequent decay. To interrogate the presence of defects, X-ray excited optical luminescence (XEOL) measurements, in which an optical spectrometer is used to observe radiative transitions in a sample following X-ray excitation, are performed. Utilizing XEOL with a third generation synchrotron light source in particular was used because it is facilitates the observation of transitions that are not observable with conventional laboratory equipment. Examples of this capability include otherwise undetected band-to-band transitions[11] and the observe a hierarchy of mid-gap defects.[12] To complement these measurements, *ab initio* density functional theory (DFT) calculations of pristine and defected BP_3N_6 were performed.

[a] *Department of Physics and Engineering Physics, University of Saskatchewan, Saskatoon, Canada*
[b] *Department of Chemistry, University of Munich (LMU), Butenandtstrasse 5-13, Munich, Germany*

Electronic Supplementary Information (ESI) available: Band structure diagram of BP_3N_6

2 Experiment and Theory

2.1 Sample Synthesis

Samples of BP_3N_6 were synthesized according to Vogel *et al.* in a high-pressure high-temperature reaction using $(PNCl_2)_3$ (abcr GmbH, 98.5%, purified by sublimation), NH_4N_3 (prepared from NH_4NO_3 (Grüssing, 99%) and NaN_3 (Acros Organics, 99%) by sublimation)[13] and *h*-BN (abcr GmbH, 99%) as starting materials.[8] The reaction conditions were achieved by a 1000 t hydraulic press (Voggenreiter) combined with a modified Walker-type module and the multianvil technique.

Stoichiometric amounts of the starting materials as well as 25wt% NH_4Cl, used as mineralizer, were ground together in a glovebox (MBraun, < 1ppm O_2/H_2O) under argon atmosphere. The powder was tightly packed into a *h*-BN-crucible (Henze), surrounded by two graphite heaters (Schunk Kohlenstofftechnik GmbH) and a ZrO_2 sleeve (Cesima Ceramics) for thermal insulation. Mo-disks (Mo 3N, 99.8%) were added each at the top and bottom of the heaters for electrical contact. The assembly was centered in a pierced octahedron (MgO, 5%-Cr_2O_3-doped, 18 mm edge length, Ceramic Substrates & Components Ltd.), which was placed into a cube of eight electrically isolated Co-doped WC-cubes (7% Co, 32 mm edge length, Hawedia) with truncated corners (11 mm edge length). The synthesis was carried out at a sample pressure of 8 GPa. The sample was heated to 1100°C within 1 h, temperature was hold for 5 h and subsequently cooled down to ambient temperature within 1 h. After decompression, all parts of the assembly were removed from the sample, which afterwards was washed with de-ionized water. BP_3N_6 was obtained as light grey powder. Phase purity was confirmed by powder X-ray diffraction.

2.2 Experimental Techniques

Samples X-ray absorption and emission spectroscopy measurements, which are sensitive to the unoccupied and occupied partial density of states of a particular element, respectively, were performed at the N K- and B K-edges. These measurements were performed at beamline 8.0.1.1 of the Advanced Light Source at Lawrence Berkeley National Laboratory.[14] These measurements are performed by promoting core electrons to the conduction band with a tunable X-ray source and monitoring their subsequent decay. X-ray absorption spectroscopy measurements were performed in total fluorescence yield mode, in which the X-ray fluorescence of the sample is monitored with a channeltron detector.[9] X-ray emission spectroscopy measurements are performed with excitation energies far above the excitation threshold,[10] with the XES spectra collected using a soft X-ray fluorescence spectrometer in a Rowland circle geometry oriented at 90 degrees with respect to the incident radiation. These measurements were performed with the sample mounted 60 degrees to the incident beam. The XAS spectra were calibrated using initial peak values of 402.10 eV and 191.80 eV in graphitic boron nitride at the N K- and B K-edges, respectively. The XES spectra were calibrated using elastic scattering features from the incident beam. The energy resolution (ΔE) of the XAS measurements was 0.10 eV, while the energy resolution of the XES measurements are 0.30 eV and 0.10 eV at the N K- and B K-edges, respectively (corresponding to resolving powers (E/ΔE) of 1300 and 2000, respectively).

X-ray excited optical luminescence measurements,[15-17] in which optical luminescence spectra are collected from a sample following X-ray excitation, were performed at the VLS-PGM beamline at the Canadian Light Source. Optical spectra were calibrated using a semiconductor laser diode.

All measurements were performed at room temperature.

2.3 Computational Methods

Samples DFT calculations for this study were performed in two steps. First, the ab initio structure of BP_3N_6 was obtained by relaxing the unit cell of the experimentally determined crystal structure of BP_3N_6 with space group $P2_1/c$ (no. 14). This work was performed using Quantum Espresso, a software package which solves the Kohn-Sham equations self consistently using a plane-wave basis and pseudopotentials.[18-19] For these calculations the generalized gradient approximation exchange correlation functional of Perdew, Burke and Ernzerhof (PBEsol) swas used with a kinetic energy cutoff of 80 Ry.[20] For structures where defects were considered, a 2 × 2 × 1 supercell was generated and the unit cell was allowed to relax. The k-mesh was selected so that the total energy per unit cell was stable to within 10^{-5} Ry, resulting in a 9 x 9 x 10 k-mesh for a single unit cell of BP_3N_6, with commensurately smaller meshes used for supercells.

For modelling the XES and XAS spectra, which are core level spectroscopy techniques, an all-electron approach is required. To this end, the commercially available WIEN2k software package, which utilized linear augmented plane waves with local orbitals in an all-electron Kohn-Sham scheme, was used to model the electronic density.[21,22] The ab initio structure calculated using Quantum Espresso was used as an input and PBEsol gradient approximation exchange correlation functional was used. Since this class of exchange-correlation functionals is known to generally underestimate the band gap of semiconductors by up to 50%,(Camargo-Martínez & Baquero, 2012; Tran & Blaha, 2009)[23,24] the modified Becke–Johnson (mBJ) exchange-correlation functional was used to calculate this parameter.[23] This is a parametrized functional which is used as a computationally inexpensive way to predict the band gap. WIEN2k was used to calculate the density of states as well as to calculate predicted XES and XAS spectra, allowing for a detailed comparison with experiment. The spectra are calculated by multiplying the PDOS with a dipole transition matrix and a radial transition probability.[25] The calculated spectra are broadened using a combination of Lorentzian and Gaussian line shapes reflecting lifetime, instrumentation and thermal broadening. The XAS and XES spectra depend on the final state of the system for that measurement,[26] which for XAS spectra corresponds to a crystal perturbed by the presence of a core hole,[26,27] which tends to shift spectral weight to lower energies. To account for this perturbation, half a core hole added to a single atom in a 2 × 1 × 1 supercell of BP_3N_6, such that core holes are separated by at least 9 Å.[28]

3 Results and Discussion

3.1 XAS and XES spectra for BP_3N_6

We begin by considering the bulk electronic properties of BP_3N_6 as interrogated by XAS and XES measurements. The experimental and calculated XES and XAS spectra of BP_3N_6 are shown in the left and right panels of Fig. 1, respectively. For each measurement type, the B K-edge and N K-edge measurements are shown in the top and bottom of each panel, respectively, each with their own corresponding energy axis, as indicated. The energy axes are aligned to the onset of spectral weight for each type of spectrum. The experimental spectra are shown in black and the calculated spectra corresponding to the ground state of the crystal are shown in blue. For the XAS spectra, which as noted above are perturbed by the presence of a core hole, a spectrum perturbed by the presence of a fractional core hole as implied by the Slater transition-state method, is shown in red.[29] The theoretical spectra were calculated using the PBEsol functional. Although the PBEsol functional used in this work is optimized to correctly calculate the structural properties of densely packed solids, it is well known that the GGA class of functionals tend to underestimate the band gap of semiconductors. To account for this, the calculated spectra have been rigidly shifted to align spectral features with experimental data. Notable features in the experimental spectra are labelled, as shown.

We start by considering the B K XES spectra in the top left of Fig. 1. The experimental spectra show four significant spectral features, labelled 1-4, which are well reproduced in the calculated ground state spectra. Considering the B K XAS spectra, shown in the top right of Fig. 1, the overall agreement between the experimental and calculated spectra is more moderate. The initial excitonic peak, (labelled a) is well represented in the calculated spectrum, but notable features at higher energies (labelled b-e) are less well represented. Features d and e appear better represented in the ground state calculation rather than the core hole calculation.

Considering the N K XES spectra, good overall agreement between the experimental data and the calculated spectra is observed. The overall spectral shape is well reproduced, with significant spectral features (labelled 5-8 in Fig. 1) being reproduced at the correct spectral position, although the experimental spectral features are less sharp than is predicted by the calculation.

Considering the N K spectra, the experimental N K XAS spectra have five significant features (labelled f-j) and generally resemble the calculated spectra. Although there is a general resemblance between the calculated spectra and experiment, considering the overall spectral strength and position of features f-j, there is much worse agreement than with the N K XES spectra. This is manifested, for example, in considering the relative intensity of features g-i compared with feature j between the experimental spectra and the core hole calculated spectrum. As with the B K XAS spectra, the initial spectral onset region is best represented by the calculated core hole spectrum

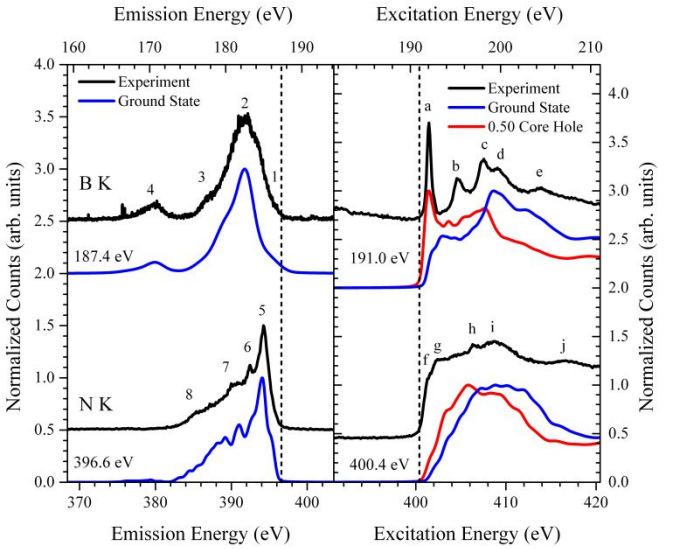

Fig. 1: (left) Experimental and calculated XES spectra with excitation energy far above excitation threshold, are shown in blue and black, respectively. (right) Experimental and calculated XAS spectra are shown, as indicated. For each panel, the B K and N K spectra are shown in the top and bottom halves of the panel, respectively, each with a corresponding energy axis. These axes are aligned to the onset of spectral weight, as indicated by the vertical dashed line with the numerical value shown for each experimental spectrum.

while beyond this region the experimental spectrum is best represented by the ground state spectrum. Comparing the calculated core hole and ground state calculations, we see that the presence of a core hole shifts spectral weight and individual features to lower energies.

The relatively moderate agreement between the theoretical and experimental XAS spectra (in contrast with the XES spectra), for both the N K- and B K-edges, suggests a limitation of the theoretical approach used herein, using a generalized gradient approximation as the exchange-correlation functional, in that it is insufficient to provide a detailed interpretation of individual features in the XAS spectra.

3.2 Band Gap of BP_3N_6

XAS and XES, which probe the occupied and unoccupied PDOS of a material, respectively, can be utilized to determine the band gap of a material. The onset of spectral weight in the XES and XAS spectra are determined using peaks in the second derivative of the spectra, a technique which allows the spectral weight onset to be reproducibly determined.[30] Other techniques, such as linear extrapolation, yield similar results. Given that the XAS spectra are perturbed by the presence of a core hole the overall band gap can only be determined from the XES-XAS separation once this perturbation has been accounted for.

Considering the B K-edge, the spectral weight onsets occur at 187.4 ± 0.1 eV and 191.0 ± 0.1 eV, yielding an overall separation of 3.6 ± 0.2 eV. Comparing the calculated ground state and core hole spectra in Fig. 1 reveals that the presence of

a core hole shifts red-shifts the onset of spectral weight by 0.3 eV, resulting in an overall band gap of 3.9 ± 0.2 eV.

Considering the N K-edge, the spectral weight onsets occur at 396.6 ± 0.3 eV and 400.4 ± 0.1 eV, yielding an overall separation of 3.8 ± 0.4 eV. Accounting for a 0.3 eV core hole shift at the N K-edge (matching the core hole shift at the B K-edge), the overall band gap as determined from the N K spectra yields a band gap of 4.1 ± 0.4 eV. Significantly, this band gap is in excellent agreement with the band gap determined by probing the B K-edge.

The experimental band gaps are compared with theory in Table 1. In this work, two exchange-correlation functionals were used, PBEsol and mBJ. The former was chosen because it is designed to calculate well the equilibrium structural properties of packed solids. It is well known however, that the general class of functionals built upon the generalized gradient approximation, tend to underestimate the electronic band gap of materials.[31] In contrast, the mBJ functional is a parametric functional which has been tuned to accurately calculate the electronic band gap.[23,24,31] In contrast with the typical behavior, the calculated PBEsol electronic band gap is 4.3 eV, which slightly overestimates the experimentally determined value. Using the mBJ exchange-correlation functional yielded an even larger band gap of 5.8 eV, significantly larger than the experimental value. With respect to the nature of the band gap, the band gap is formally indirect (shown Fig. S1 of the supplementary information), with the conduction band minimum occurring between the Z and Gamma points, while the valence band maximum is at the D point. The conduction and valence bands are sufficiently dispersive that the minimum momentum conserving transition from the valence to conduction band is within 40 meV of the formal electronic band gap.

3.3 Mid-gap Defects

The overall electronic properties of a material, and its operation in a potential device, depend not only on bulk parameters like the band gap, but can be greatly perturbed by the presence or absence of mid-gap defects. To interrogate these defects, XEOL measurements were performed. In this work the sample is irradiated with 160 eV photons and the luminescence spectra are collected with an optical spectrometer. The resulting spectrum is shown in Fig. 2. This spectrum can be decomposed into four constituent Gaussian features centered at 2.81 eV, 3.12 eV, 3.68 eV and 3.95 eV. Gaussian features were utilized due to vibrational and inhomogeneous broadening.

The lowest energy feature at 2.81 eV has a full-width half-maximum (FWHM) of 0.97 eV, with the other features having a FWHM ranging between 0.27 eV and 0.37 eV. All of these

Table 1: Experimental and calculated band gaps. The experimental band gaps are denoted by Δ_{exp}, calculated band gaps are denoted by Δ_{PBEsol} and Δ_{mBJ}.

Compound	Δ_{exp} [eV]	Δ_{mBJ} [eV]	Δ_{PBEsol} [eV]
BP_3N_6	3.9 ± 0.2 eV (B K) 4.1 ± 0.4 eV (N K)	5.8	4.3

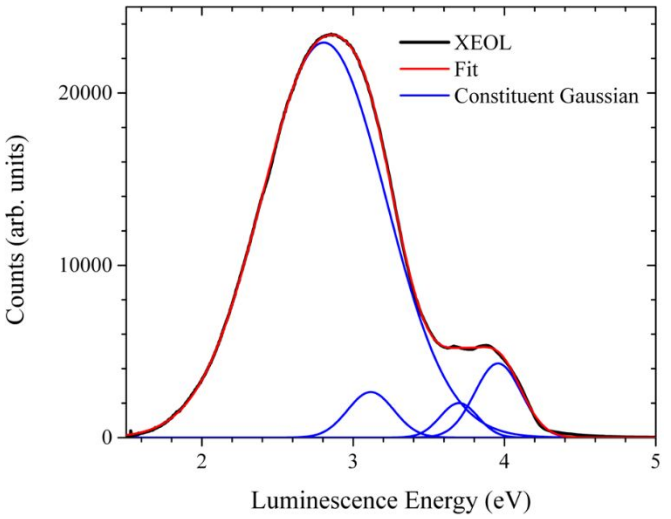

Fig. 2: Optical luminescence spectrum of BP_3N_6 under 160 eV X-ray irradiation. The measured spectrum can be decomposed into four Gaussian features, as shown.

energies are less than the electronic band gap, and as such no band-to-band recombination was observed.

To better understand the origin of the observed luminescence, 2 × 2 × 1 supercells of BP_3N_6 defected with nitrogen vacancies at each of the unique crystallographic nitrogen site were considered (corresponding to one vacancy per 160 atoms). The total DOS per unit cell for pristine and N_v defected BP_3N_6 are shown in the right panel of Fig. 3. In this panel, the energy axis is relative to the highest occupied level of pristine BP_3N_6, with the defected cells energies shifted to align the top of the valence band. The Fermi energy level for the defected unit cells are indicated with a dashed horizontal line, which matches the color of the underlying curve. Each nitrogen vacancy supercell yields a distinct total DOS, and the Fermi energy level for each unit cell corresponds to a 50% occupation of the lowest energy mid-gap band. Considering the DOS of the defected cells in aggregate, the mid-gap defect levels tend to cluster around four specific energy levels, which are shown schematically in the left panel Fig. 3. The lowest energy mid-gap levels are clustered within ~0.6 eV of each other, while the other mid-gap levels are much closer in energy. Considering that the total energy of each defected unit cell is within ~0.1 Ry of each other, if nitrogen vacancies are present, then they might be expected to be present without preferentially forming at a specific crystallographic site. Formation energies for each modelled defect are provided in the Supplemental Information.

Putting this together, we now show how the calculated band diagram shown in the schematic can be used to rationalize the

observed XEOL spectrum by considering possible carrier trapping and recombination in BP_3N_6. Following X-ray excitation, injected carriers are initially in an excited state. Following excitation, they relax to the conduction and valence band edges. Once at the band edges the carriers can recombine by various mechanisms, including via the mid-gap trap states caused by the presence of nitrogen vacancies. For sufficient carrier densities, radiative recombination of carriers in these mid-gap trap states to the valence band would be observed. Such transitions are shown schematically in the left panel of Fig. 3. Notably, for a system with nitrogen vacancies, this would lead to four principal radiative features, with the lowest

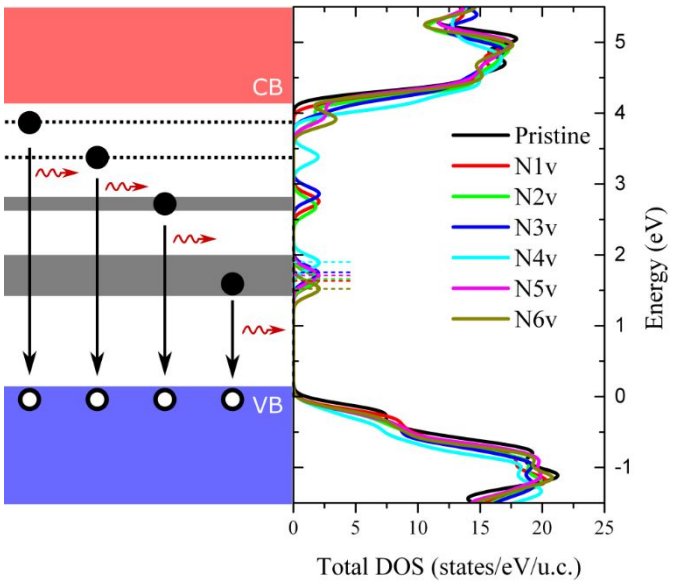

Fig. 3: (left) Schematic representation of the band diagram of BP_3N_6 with nitrogen vacancies. Possible radiative transitions of injected carriers are shown. (right) Total DOS of BP_3N_6 unit cells for pristine and defected cases, as indicated. For supercells, this was normalized to the total DOS for a primitive unit cell. The energy axis corresponds to the highest occupied energy level of the pristine cell, with the energy of the defected cells shifted so that the top of the valence bands are aligned. For these cells, the Fermi energy is indicted with a horizontal dashed line in the corresponding color, as indicated.

energy feature being broadened by the formation of a broad mid-gap band associated with energetically overlapping (but not aligned) mid-gap states. This is consistent with the experimental XEOL spectra, in which four spectral features are observed, all significantly less than the band gap and with the lowest energy feature being significantly broader than the others. Notably, in making this comparison, we do not compare the absolute energy of the experimental features with the energy separation between mid-gap states in the calculated supercells. This is because the exchange-correlation functional used to perform these calculations, PBEsol, is well known to poorly describe the magnitude of gaps between different bands (despite describing the bands themselves well). As such, the energy separations between mid-gap defect states are not expected to be accurate, but the hierarchy of the resulting mid-gap levels is anticipated to be schematically correct.

Conclusions

The electronic properties of BP_3N_6, synthesized under high-pressure high-temperature conditions, have been studied experimentally and theoretically. Considering the bulk properties of this material, the band gap has been determined to be 3.9 ± 0.2 eV and 4.1 ± 0.4 eV at the B K- and N K-edges, respectively. This contrasts with calculated predicted band gaps of 4.3 eV and 5.8 eV calculated using the PBEsol and mBJ exchange-correlation functionals, respectively. The band gap is predicted to be indirect. Upon X-ray irradiation optical luminescence of the BP_3N_6 sample was observed. Reconciling the observed luminescence with DFT calculations suggests that the mid-gap defect energy levels responsible for this luminescence are attributed to the presence of nitrogen vacancies.

Conflicts of interest

There are no conflicts to declare.

Acknowledgements

M.F.A.F. is grateful to the University of Saskatchewan, Canada for the Dean's scholarship. We also acknowledge the support from the Natural Sciences and Engineering Research Council of Canada (NSERC) and the Canada Research Chair Program. Experiments for this work were performed at the Canadian Light Source (CLS) in Saskatoon and the Advanced Light Source (ALS) in Berkeley, USA. CLS is funded by the Government of Canada, NSERC, National Research Council (NRC), Canadian Institutes of Health Research (CIHR), the Government of Saskatchewan, and the University of Saskatchewan. The ALS is financed by the Director, Office of Science, Office of Basic Energy Sciences, of the US Department of Energy under contract No. DE-AC02-05CH11231. In addition, we are also thankful to Compute Canada for computational resources. W.S. and S.A. furthermore acknowledge financial support by the Deutsche Forschungsgemeinschaft (DFG, German Research Foundation) under Germany's Excellence Strategy – EXC 2089/1–390776260 and DFG-Project SCHN 377/18-1.

References

1 W. Schnick, *Angew. Chem. Int. Ed. Engl.,* 1993, **32**, 806-818.
2 H. Lange, G. Wötting and G Winter, ," *Angew. Chem. Int. Ed. Engl.*, 1991, **30**, 1579-1597.
3 O. O. Kurakevych, *J. Superhard Mater.*, 2009, **31**, 139-157.
4 Y. Hirota, and T. Kobayashi, *" J. Appl. Phys.*, 1982, **53**, 5037-5043.
5 M. S. Choudhary, J. K. Fink, K. Lederer and H. A. Krässig, 1987, **55**, 863–869.
6 E.-C. Koch and S. Cudzito, *Angew. Chemie Int. Ed.*, 2016, **55**, 15439–15442.
7 H. P. Baldus, W. Schnick, J. Luecke, U. Wannagat and G. Bogedain, *Chem. Mater.*, 1993, **5**, 845–850.

8 S. Vogel, A. T. Buda and W. Schnick, *Angew. Chem. Int. Ed.*, 2018, **57**, 13202–13205.
9 J. Yano and V. K. Yachandra, *Photosynth. Res.*, 2009, **102**, 241–254
10 U. Bergmann and P. Glatzel, *Photosynth. Res.*, 2009, **102**, 255–266.
11 T. M. Tolhurst, P. Strobel, P. J. Schmidt, W. Schnick, and A. Moewes, *Chem. Mater.*, 2017, **29**, 7976–7983.
12 T. de Boer, J. Häusler, P. Strobel, T. D. Boyko, S. S. Rudel, W. Schnick and A. Moewes, *J. Phys. Chem. C*, 2021, **125**, 27959.
13 W. J. Frierson, *Inorg. Synth.*, 1946, **8**, 136.
14 J. J. Jia, T. A. Callcott, J. Yurkas, A. W. Ellis, F. J. Himpsel, M. G. Samant, J. Stöhr, D. L. Ederer, J. A. Carlisle, E. A. Hudson, L. J. Terminello, D. K. Shuh and R. C. C. Perera *et al.*, *Rev. Sci. Instrum.*, 1995, **66**, 1394–1397.
15 A. Goulon and J. Rogalev, "X-ray Excited Optical Luminescence Spectroscopies," in *Chemical Applications of Synchrotron Radiation, Part II: X-ray Applications*, T. K. Sham, Ed. World Scientific, 2002.
16 T. K. Sham, R. Sammynaiken, Y. J. Zhu, P. Zhang, I. Coulthard and S. J. Naftel, *Thin Solid Films*, 2000, **363**, 318–321.
17 R. A. Rosenberg, Y. Choi, K. Vijayalakshmi, M. Kareev, J. Tchakhalian, Snjezana Balaz, and L. J. Brillson., *Appl. Phys. Lett.*, 2013, **102**, 192910.
18 P. Giannozzi *et al.*, "QUANTUM ESPRESSO: a modular and open-source software project for quantum simulations of materials," *J. Phys. Condens. Matter*, vol. 21, no. 39, p. 395502 (19pp), 2009, [Online]. Available: http://www.quantum-espresso.org.
19 P. Giannozzi *et al.*, *J. Phys. Condens. Matter*, 2017, **29**, 465901.
20 J. P. Perdew, A. Ruzsinszky, G. I. Csonka, O. A. Vydrov, G. E. Scuseria, L. A. Constantin, X. Zhou and K. Burke. *Phys. Rev. Lett.*, 2008, **100**, 136406.
21 P. Blaha et al., WIEN2k, An Augmented Plane Wave + Local Orbitals Program for Calculating Crystal Properties, 2018th ed. Wien: Techn. Universität Wien.
22 P. Blaha, K. Schwarz, F. Tran, R. Laskowski, G. K. H. Madsen and L. D. Marks, *J. Chem. Phys.*, 2020, **152**, 074101.
23 F. Tran and P. Blaha, *Phys. Rev. Lett.*, 2009, **102**, 226401.
24 J. A. Camargo-Martínez and R. Baquero, *Phys. Rev. B*, 2012, **86**, 195106.
25 K. Schwarz, A. Neckel and J. Nordgren, *J. Phys. F Met. Phys.*, 1979, **9**, 2509–2521.
26 G. Mahan, *Phys. Rev. B*, 1980, **21**, 1421–1431.
27 U. von Barth and G. Grossmann, *Phys. Rev. B*, 1982, **25**, 5150–5179.
28 A. R. Williams, R. A. DeGroot and C. B. Sommers, *J. Chem. Phys.*, 1975, **63**, 628–631.
29 D. A. Liberman, *Phys. Rev. B*, 2000, **62**, 6851–6853.
30 E. Z. Kurmaev, R. G. Wilks, A. Moewes, L. D. Finkelstein, S. N. Shamin and J. Kuneš, *Phys. Rev. B*, 2008, **77**, 165127.
31 P. Borlido, J. Schmidt, A. W. Huran, F. Tran, M. A. L. Marques and S. Botti, *npj Comput. Mater.*, 2020, **6**, doi: 10.1038/s41524-020-00360-0.